Methicillin treatment reveals that FtsZ phosphorylation influences the cell division of Streptococcus pneumoniae

PNAS Nexus, 2026, **5**, pgag200
https://doi.org/10.1093/pnasnexus/pgag200
Published: 4 June 2026
Research report

Methicillin treatment reveals that FtsZ phosphorylation influences the cell division of *Streptococcus pneumoniae*

Sathya Narayanan Nagarajan[1,6], Sylvie Manuse[1,6], Dimitri Juillot[2], Léo Claude[1], Vaishnavi Ravikumar[3,4], Emmanuelle Neumann[5], Jean-Pierre Lavergne[1], Mirita Franz-Wachtel[4], Boris Macek[4], Ivan Mijakovic[3], Cecile Morlot[5], Rut Carballido-Lopez[2], and Christophe Grangeasse[1]*

[1]Molecular Microbiology and Structural Biochemistry, UMR 5086, Université Claude Bernard Lyon 1, CNRS, 69007 Lyon, France
[2]INRAE, AgroParisTech, Micalis Institute, Université Paris-Saclay, 78350 Jouy-en-Josas, France
[3]Department of Biology and Biological Engineering, Chalmers University of Technology, 412 96 Gothenburg, Sweden
[4]Department of Quantitative Proteomics, Institute for Cell Biology, University of Tübingen, 72074 Tübingen, Germany
[5]CNRS, CEA, IBS, Université Grenoble Alpes, F-38000 Grenoble, France
*To whom correspondence should be addressed: Email: christophe.grangeasse@cnrs.fr
[6]S.N.N. and S.M. contributed equally to this work.
Edited By Ian Wilson

Abstract

Protein phosphorylation plays a crucial role in regulating cell division and morphogenesis in many bacteria. In *Streptococcus pneumoniae*, the serine/threonine kinase StkP orchestrates cell wall assembly and cell morphogenesis by phosphorylating several proteins involved in cell division. In this study, we provide evidence that FtsZ, a conserved tubulin-like protein that coordinates pneumococcal cell elongation and constriction, is phosphorylated in vivo by StkP at six threonine residues within its C-terminal linker (CTL). Mutational analysis reveals the structural role of the CTL in pneumococcal cell division and further shows that its phosphorylation status influences cell morphogenesis. Importantly, phosphomimetic FtsZ mutants rescue division blocks induced by sublethal concentrations of methicillin, which targets the essential septal cell wall synthase PBP2x. Additionally, we demonstrate that CTL phosphorylation affects FtsZ polymerization and filament bundling in vitro. It also accelerates FtsZ treadmilling dynamics and alters its interactome in vivo. Altogether, these findings support a model in which CTL phosphorylation fine-tunes FtsZ filament dynamics to sustain cell division under β-lactam stress, representing a potential adaptive mechanism for antibiotic tolerance.

Keywords protein phosphorylation, FtsZ, cell division, peptidoglycan, *Streptococcus pneumoniae*

Significance statement

Adapting to the environmental conditions is indispensable for the evolution and survival of bacterial species. Besides genome modifications that confer heritable traits, nongenetic and nonheritable adaptive changes are also critical. In this work, we propose that serine/threonine phosphorylation enhances nonheritable phenotypes through posttranslational modifications in response to survival challenges, particularly those induced by antibiotic exposure. Our findings demonstrate that the phosphorylation of the key cell division protein FtsZ, specifically within its flexible C-terminal linker, mitigates cell division impairment when exposed to methicillin, a β-lactam antibiotic that inhibits the septal peptidoglycan biosynthesis. Our work thus uncovers a previously unrecognized role for phosphorylation in the intrinsically disordered region of FtsZ, modulating its biophysical properties and interactome to support bacterial adaptation under stress.

Received: June 16, 2025. **Accepted:** May 21, 2026

Introduction

The eukaryotic-like tubulin protein FtsZ is pivotal to the process of cell division in the vast majority of bacterial species (1, 2). FtsZ undergoes continuous GTP-dependent polymerization and depolymerization throughout the cell. At the division site, these filaments coalesce into an apparent ring-like structure, known as the Z-ring (3, 4). Cryo-electron tomography studies showed that the Z-ring can form a continuous, though nonhomogeneous, band of overlapping FtsZ filaments in vivo (5). The Z-ring was further shown to form a dynamic and discontinuous structure with a patchy and heterogeneous distribution of FtsZ filaments that treadmill around the cell (6–8). The Z-ring serves as a scaffold for the recruitment and assembly of the divisome, the protein machinery responsible for cell division (9, 10). The N-terminal GTPase domain of FtsZ is linked via an intrinsically disordered linker (C-terminal linker, CTL) to a conserved C-terminal peptide (CTC), which mediates interactions with key division proteins such as the membrane-anchored FtsA (11, 12).

While the functions of the GTPase domain and CTC have been well characterized, the role of the CTL has only recently been investigated (13–15). The CTL is a flexible, intrinsically disordered region (IDR) that varies significantly in length and sequence across bacterial species, lacking conserved motifs and structural organization (11, 16). IDRs are known to serve a versatile range of regulatory functions. For example, they can confer molecular flexibility, promote liquid–liquid phase separation, and participate in diverse protein–protein interactions (17–19). Some properties of the CTL are thus proposed to be encoded via evolutionarily conserved, nonrandom sequence patterns that help mediate autoregulatory interactions between covarying regions within FtsZ (20). For instance, changes in the amino acid composition of the CTL domain are tolerated in both *Bacillus subtilis* and *Escherichia coli*, while still providing the CTL peptide disorderliness (13, 14). In contrast, the functional replacement of the CTL in *Caulobacter crescentus* from a different species compromises its growth and cell shape (15). Deletion of the CTL in *E. coli*, *B. subtilis*, or *C. crescentus* results in severe division defects, including cell filamentation, cell bulging, and lysis, respectively, due to the formation of nonfunctional Z-rings (13–15). In vitro, structural studies further demonstrate that the loss of the CTL domain alters the bundling properties, size, and thickness of FtsZ filaments (21). In *C. crescentus*, the CTL domain is implicated in modulating the lateral interactions between the filaments (21). In addition, biophysical analyses demonstrate that FtsZ protofilaments self-organize into loosely bundled assemblies in solution, with the CTL domain acting as a spacer that modulates lateral filament interactions and limits excessive bundling (22).

Streptococcus pneumoniae is a prominent model for studying bacterial cell division and FtsZ function (10). This gram-positive bacterium exhibits an ovoid cell shape and divides by binary fission. In rod-shaped bacteria, cell elongation relies on sidewall synthesis by the elongasome, a protein complex scaffolded by the actin homolog MreB along the lateral region of the cell (23). *Streptococcus pneumoniae* lacks MreB, and the Z-ring recruits primary elongation and division proteins early in the cell cycle (24, 25). Consequently, the divisome coordinates both cell elongation and division (10, 25–27). The dynamic treadmilling of FtsZ filaments, characterized by polymerization at one end and depolymerization at the other end (6, 7, 28, 29), subsequently distributes the divisome components around the division site, guiding septal wall synthesis (23–25). Unlike rods that elongate through dispersed expansion of their lateral wall, pneumococcal cells elongate through zonal cell wall synthesis at the periphery of the septum, where the elongasome remodels the septal wall (10, 25–27). In ovococci, cell shape and elongation thus depend on the coordinated activity of both the divisome and the elongasome, both of which are functionally intertwined with FtsZ dynamics. While FtsZ treadmilling and divisome assembly have been well characterized, the role of the CTL in this context remains unknown.

Phosphoproteomics studies have identified phosphorylation sites within the FtsZ CTL in *S. pneumoniae* (30–33), echoing similar findings in other bacteria (34–36). The functional relevance of these modifications, however, remains enigmatic. *S. pneumoniae* encodes a single Ser/Thr kinase (StkP) (37–39), which phosphorylates multiple proteins (40, 41) involved in cell division and morphogenesis, including DivIVA (38, 42), the PBP2a regulator MacP (43), the division site selection protein MapZ (44, 45), the cell elongation regulator EloR (also known as KhpB or Jag) (46–48), and the chromosome segregation regulator RocS (49). Given that phosphorylation is known to modulate the biochemical properties and function of IDRs (50, 51), the pneumococcus therefore represents an ideal organism to investigate the regulatory role of FtsZ CTL phosphorylation and better characterize the molecular mechanisms underlying cell division in the pneumococcus.

In this study, we demonstrate that the CTL of *S. pneumoniae* FtsZ is required for cell morphogenesis and division, and undergoes phosphorylation in vivo. We identify the CTL phosphorylation sites, characterize their impact on FtsZ biochemical properties and dynamics, and assess their contribution to cell division. Importantly, our work reveals that CTL phosphorylation plays a vital role under β-lactam stress that hampers cell wall assembly. Our observations suggest a model in which phosphorylation of the CTL region modulates FtsZ activity to facilitate cell constriction and successful division under challenging conditions.

Results

The CTL of FtsZ is essential for cell division and morphogenesis

To investigate the role of the intrinsically disordered, CTL of FtsZ in *S. pneumoniae*, we constructed a series of mutant strains with sequential deletions of various segments of the CTL (Fig. 1a). Throughout our study, all mutant alleles were integrated at the endogenous chromosomal locus and expressed from the native promoter, ensuring physiological expression levels and serving as the sole source of protein. Western blot analysis confirmed that the steady-state levels of FtsZ of all CTL deletion variants were comparable to wild-type (WT) FtsZ (Fig. S1a). Deletions were classified by their position along the CTL: ΔC1 and ΔC2 targeted the N-terminal region, while ΔC3 and ΔC4 removed segments from the C-terminus (Fig. 1a). Since complete CTL deletion was not viable, confirming it is critical for FtsZ function, we constructed a ΔC5 mutant lacking the central CTL segment (Fig. 1a). Microscopy analysis revealed that all the CTL deletion mutants, except ΔC2, exhibited significant morphological defects such as minicell formation and bulging. The ΔC2 mutant

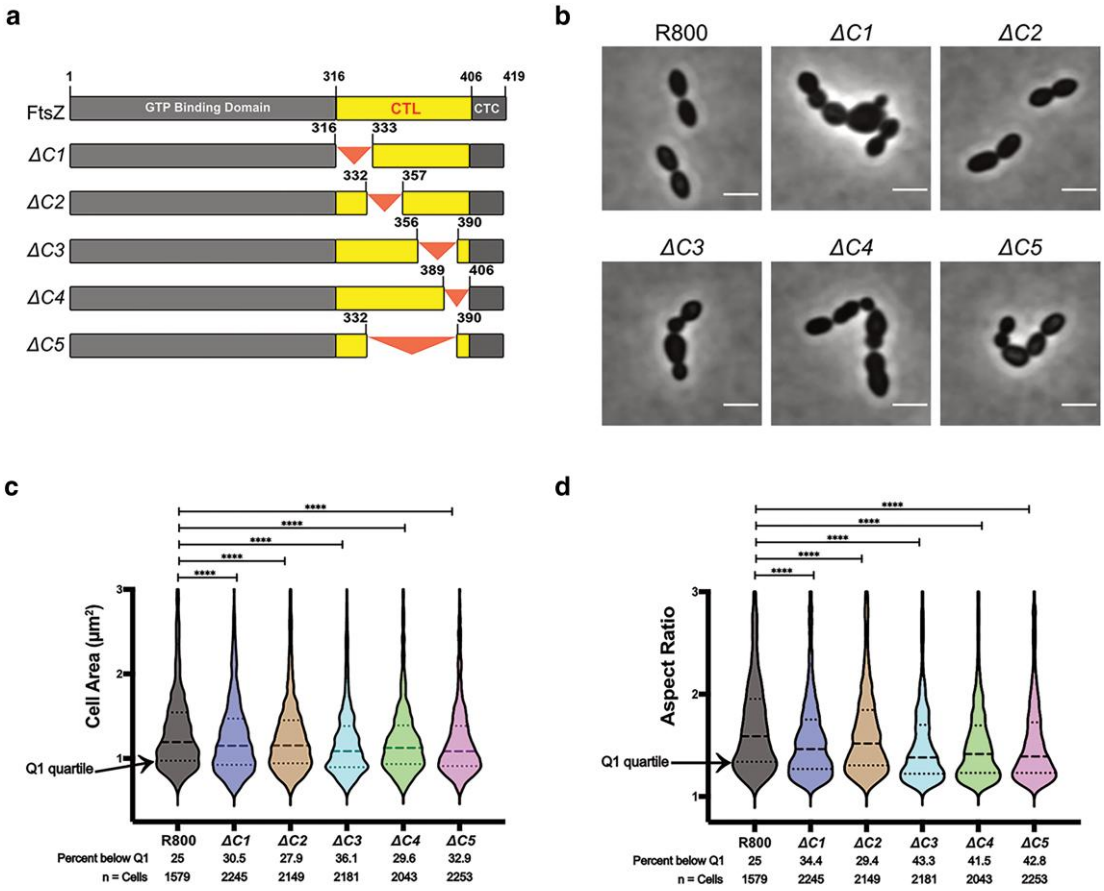

Figure 1 The CTL of FtsZ plays a vital role in cell division. a) Schematic representation of FtsZ and the C-terminal deletion variants (CTL). The core GTP-binding domain and the C-terminal conserved peptide (CTC) are depicted in gray, while the CTL is illustrated in yellow. The region of the CTL domain containing amino acid deletions is marked with an inverted red arrow, designating the CTL variants ΔC1 through ΔC5. b) Phase-contrast microscopy images show representative images of R800 (WT), Δ*C1*, Δ*C2*, Δ*C3*, Δ*C4*, and Δ*C5* cells (scale bar, 1 μm). c) A violin plot illustrates each strain's cell area (μm^2). d) A violin plot displays the cell aspect ratio distribution for each strain, as determined by the ratio of the cell length along its central axis to its width measured perpendicularly. A high aspect ratio indicates an elongated cell, while a low aspect ratio suggests a spherical cell. In c and d, an arrow shows the Q1 quartile, with the percentage of the population within it for WT and CTL deletion variants. A two-tailed *P*-value calculated through a nonparametric Mann–Whitney test indicates ****$P < 0.0001$. The letter "*n*" represents the number of cells analyzed, and data from three independent experiments are included.

displayed only minor morphological differences compared with the WT strain (Fig. 1b). Our quantitative morphometric analysis revealed that the CTL deletion mutants exhibited a significant increase (30–36%) in the prevalence of smaller-sized cells, with many cells falling below the first quartile (Q1) compared with WT cells (Fig. 1b and c). Additionally, we evaluated the distribution of aspect ratios, which indicate the ratio between cell length and width, to assess cell elongation or bulging within the population. In contrast to the WT, 30–44% of the CTL variants exhibited aspect ratios below the first quartile (Q1) of WT cells, indicating that these cells displayed aberrant shapes (Fig. 1b and d). These results highlight the crucial role of the FtsZ CTL in maintaining proper cell shape and division in *S. pneumoniae*.

CTL phosphorylation and impact on cell shape, FtsZ dynamics, and peptidoglycan assembly

The phosphorylation of the C-terminal flexible linker in FtsZ was first identified through phosphoproteomic analyses in *Mycobacterium tuberculosis* and *B. subtilis* (34, 35). Subsequent phosphoproteomic studies also detected phosphorylated FtsZ in *S. pneumoniae* (31, 32). Nevertheless, the functional relevance of this modification remains largely unexplored. Using an *ftsZ-mGfp* strain (25) grown under normal conditions and a GFP-trap resin to immunoprecipitate FtsZ-mGFP, followed by liquid chromatography-mass spectrometry (LC-MS) analysis, we identified six phosphorylated threonine residues in the CTL (Fig. S2a–h), including the previously reported sites T333, T338, T356, and T388 (31–33). To assess the overall effect of CTL phosphorylation, we generated phosphoablative (*ftsZ-TA*) and phosphomimetic (*ftsZ-TE*) mutants by substituting all six threonine residues with either alanine or glutamic acid, respectively (Fig. 2a). FtsZ protein levels remained unchanged in these mutants (Fig. S3a) and growth curves were similar to those of WT cells (Fig. 2b). Nonetheless, the *ftsZ-TE* mutant showed a slight, yet significant, difference in size distribution: 33.1% of *ftsZ-TE* cells fell within the Q1 quartile of WT cell area, while these small-sized cells only represented 25 and 26.4% of WT and *ftsZ-TA* cells, respectively (Fig. 2c and d). Unlike the CTL deletion mutants that produce minicells (Fig. 1b), neither the *ftsZ-TA* nor the *ftsZ-TE* phosphomutants formed minicells under our experimental conditions.

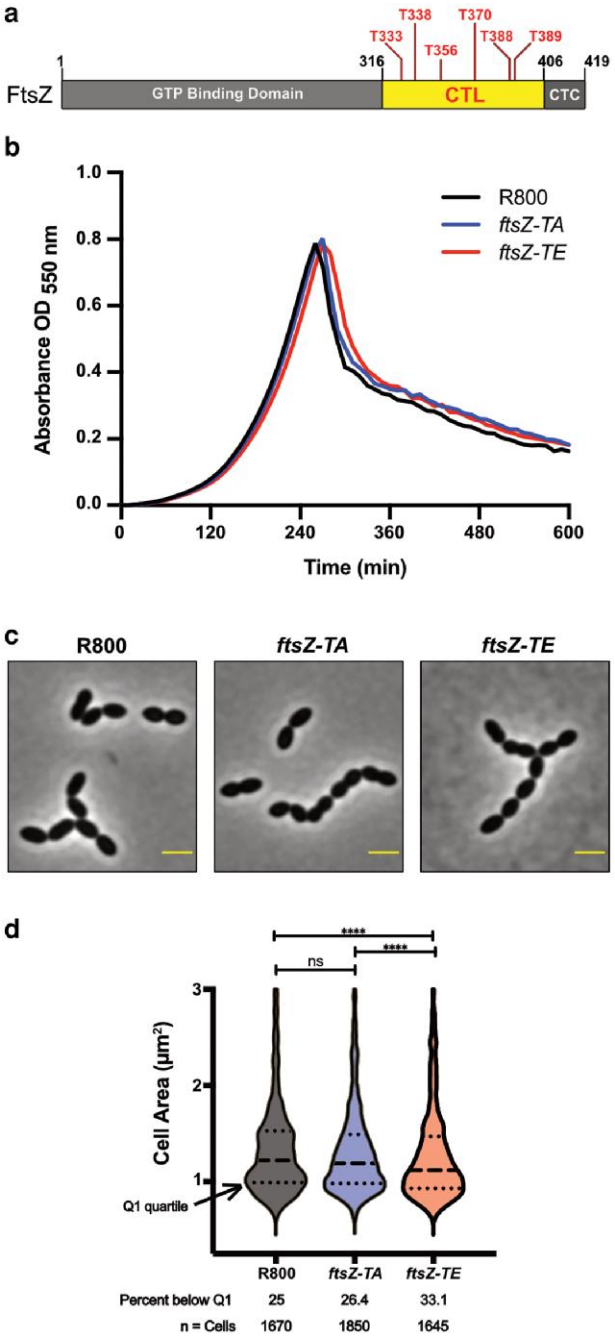

Figure 2 Phosphorylation of the CTL influences cell shape. a) A schematic representation of FtsZ highlighting the phosphorylated threonine residues in the CTL. b) Growth curves of WT and phosphomutant variant (*ftsZ-TA* and *ftsZ-TE*) strains. c) Phase-contrast microscopy images illustrate representative images of WT, phosphoablative *ftsZ-TA*, and phosphomimetic *ftsZ-TE* cells (scale bar, 1 μm). d) Violin plot depicting cell area distribution (μm^2) for each strain. An arrow shows the Q1 quartile, with the percentage of the population within it for the WT and phosphomutant variants. A two-tailed *P*-value, determined through a nonparametric Mann–Whitney test, shows ****$P < 0.0001$ and ns for $P = 0.126$. The letter "*n*" represents the number of cells analyzed, with data drawn from three independent experiments.

Instead, the *ftsZ-TE* mutant exhibited a mild phenotype characterized by a decreased cell area. These findings suggest that permanent phosphorylation of FtsZ CTL affects pneumococcal cell morphology and that CTL phosphorylation modulates cell shape homeostasis.

To assess whether TA and TE substitutions influence FtsZ localization, we constructed two strains in which the native *ftsZ* gene was replaced with *ftsZ-TA-mGfp* or *ftsZ-TE-mGfp* gene fusions. We verified that the levels of FtsZ-TA-mGFP and FtsZ-TE-mGFP were similar to those of FtsZ-mGFP (Fig. S3b). Like FtsZ-mGFP (44), FtsZ-TA-mGFP and FtsZ-TE-mGFP localized to the parental division site and daughter-cell equators (Fig. 3a). However, after sorting the cells according to their length, heat maps showed that in late-division cells, slightly more FtsZ-mGFP was detected at the parental division site of WT cells compared with the TA and TE variants (Fig. 3b). Therefore, expression of phosphoablative and phosphomimetic variants affects FtsZ localization in a very subtle manner. We also assessed whether phosphorylation altered peptidoglycan (PG) synthesis using pulse-labeling with a fluorescent D-alanine derivative (BADA) (53) (Fig. 3c). Cell-cycle resolved heat maps showed that WT, *ftsZ-TA*, and *ftsZ-TE* strains exhibited similar PG synthesis patterns, with strong septal and weak equatorial fluorescence signals (Fig. 3c and d). Altogether, these results indicate that CTL phosphorylation does not affect PG synthesis but does slightly affect pneumococcal cell shape and FtsZ localization under normal laboratory growth conditions.

CTL phosphorylation suppresses the cell division block under methicillin stress

The higher proportion of smaller cells observed in the *ftsZ-TE*-mutant (Fig. 2c and d) led us to hypothesize that CTL phosphorylation might influence the balance between cell elongation and division. As methicillin is a β-lactam antibiotic that explicitly inhibits the cell wall synthase PBP2x required for pneumococcal division (27, 28, 54), we wondered whether it could be used to reveal the function of CTL phosphorylation in cell morphogenesis. To investigate this, we treated WT, *ftsZ-TA*, and *ftsZ-TE* cells with sublethal concentrations of methicillin. As shown in Fig. 4a, methicillin induced the early lysis of all three strains (Fig. 4a). Microscopy further revealed that WT cells displayed cell elongation typical of a division block observed in the presence of β-lactam antibiotics (Fig. 4b and c). More precisely, WT cells grown in the absence of methicillin exhibited only 25% of cells (above Q3 quartile) exceeding 1.37 μm in length.

In contrast, ∼50% of the WT cells showed a cell area distribution above this threshold under methicillin stress. A similar observation was made for the phosphoablative *ftsZ-TA* mutant, with ∼56% of the population falling within the Q3 quartile (Fig. 4b and c) in the presence of methicillin. In stark contrast, the phosphomimetic *ftsZ-TE* mutant, grown in the presence of methicillin, exhibited a markedly different behavior than the WT and *ftsZ-TA* strains, with fewer than 37% of the cells falling within the Q3 quartile (Fig. 4b and c). To rule out any effect of methicillin on FtsZ production or stability, we confirmed that FtsZ levels remained stable across strains, regardless of methicillin presence (Fig. S4a). Importantly, these phenotypes cannot be attributed to differences in the minimum inhibitory concentration (MIC) between the *ftsZ* mutants and the WT strain, as the MIC was identical across all strains (0.250 μg mL^{-1}). These data indicate that phosphomimetic CTL mutations significantly rescue the cell division block caused by methicillin.

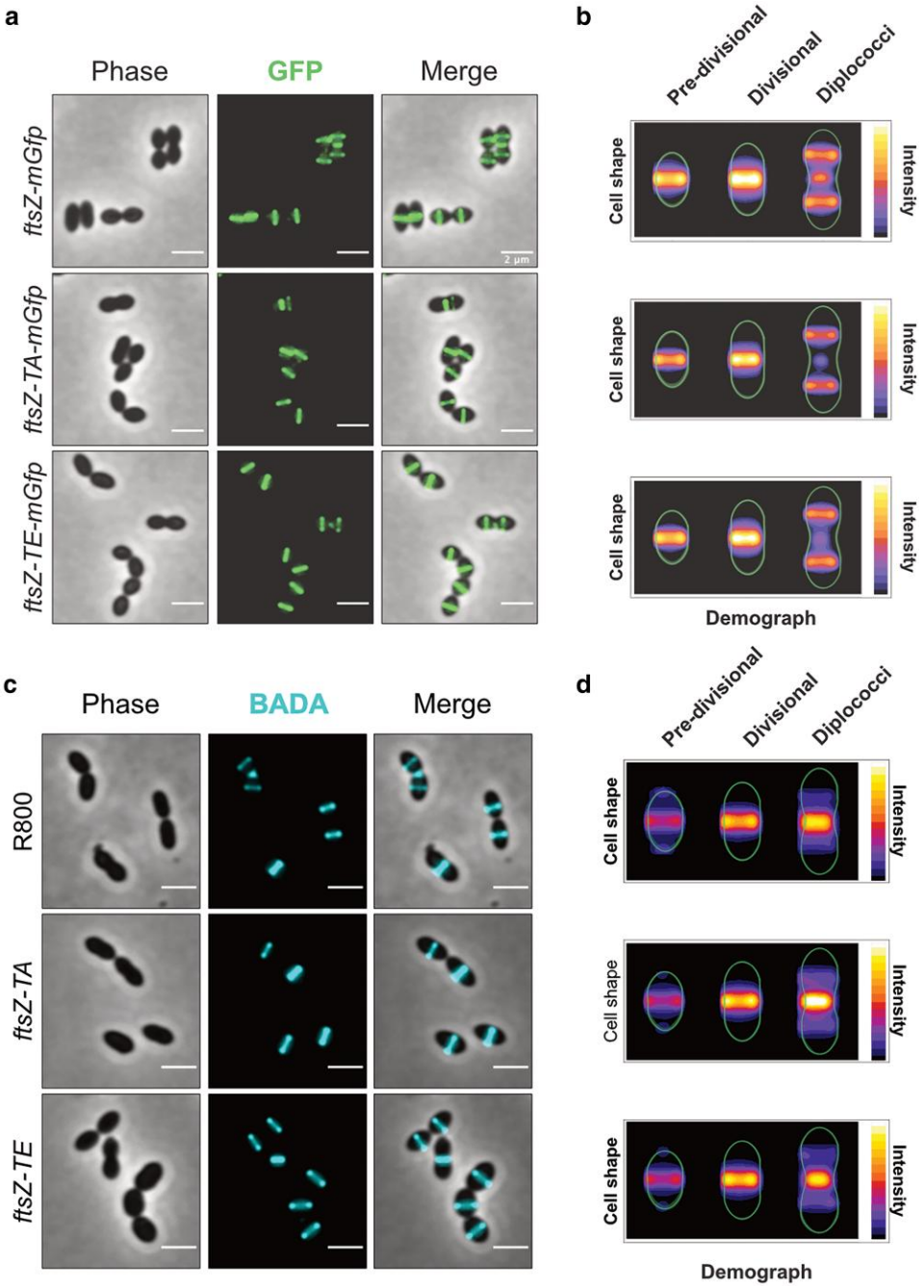

Figure 3 CTL phosphorylation does not affect FtsZ localization or PG synthesis. a. FtsZ localization in WT, phosphoablative, and phosphomimetic mutants is examined using mGFP fusions. The left panel shows phase-contrast images, the middle panel presents GFP fluorescence, and the right panel features merged phase-contrast and GFP images (scale bar, 2 μm). b) Cells are categorized into predivisional, divisional, and diplococci based on their length. Heat maps illustrate the localization of FtsZ-mGFP in WT and phosphomutant strains. Images are derived from a single experiment, and results are consistent with three independent experiments. c) To visualize PG synthesis, growing cells of R800 (WT) and phosphomutants were pulse labeled with D-amino acid analog BADA (52). The left panel shows phase-contrast images of WT, phosphoablative *ftsZ-TA*, and phosphomimetic *ftsZ-TE*. The middle panel shows BADA-stained images; the right panel presents merged phase-contrast and BADA images (scale bar, 2 μm). Cells are categorized into predivisional, divisional, and diplococci based on their cell length. The heat map depicts PG synthesis in WT and phosphomutant strains. Images are derived from a single experiment and are consistent with observations from two independent experiments.

To determine which CTL phosphorylation sites contribute to cell-division modulation, we examined a series of *ftsZ-TA* and *ftsZ-TE* mutants carrying single, dual, triple, tetra, and hexa substitutions (Fig. S5a and b). These strains were grown under sublethal methicillin stress and analyzed for their ability to alleviate the division block (Fig. S5a and b). In the presence of methicillin, WT cells exhibited ∼69% of the population above the Q3 quartile, consistent with elongation due to impaired constriction. None of the phosphoablative *ftsZ*-TA mutants showed any rescue of this phenotype, displaying Q3 distributions comparable to WT (Fig. S5a). Lower-order phosphomimetic *ftsZ-TE* mutants (single to triple) likewise failed to alter the methicillin-induced shift in cell-size distribution (Fig. S5b). In contrast, tetra and hexa *ftsZ-TE* mutants exhibited a marked improvement, with

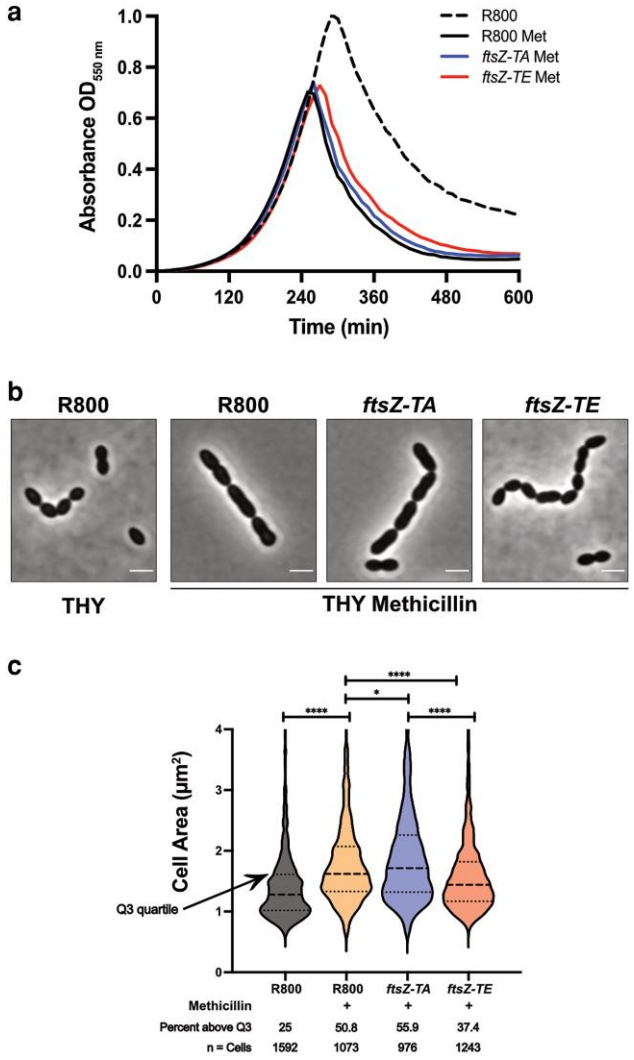

Figure 4 Impact of methicillin treatment on cell growth and shape of *ftsZ* phosphomutants. a) Growth curves of WT and phosphomutant strains in the absence or the presence of 50 ng mL^{-1} methicillin. b) Representative phase-contrast microscopy images of WT, phosphoablative *ftsZ-TA*, and phosphomimetic *ftsZ-TE* cells cultivated in the absence or the presence of 50 ng mL^{-1} methicillin (scale bar, 1 μm). Cells were harvested for this analysis ∼120 min after methicillin addition (OD_{550} = 0.10–0.15), before the onset of autolysis shown in (a) (240 min). c) Violin plots showing the distribution of cell area (μm^2) for each strain. An arrow indicates the Q3 quartile, with the percentage of the population exceeding it for the WT and phosphomutant variants. A two-tailed *P*-value, derived from a nonparametric Mann–Whitney test, indicates ****$P < 0.0001$ and *$P = 0.0259$. The letter "*n*" denotes the number of cells analyzed, with data collected from three independent experiments.

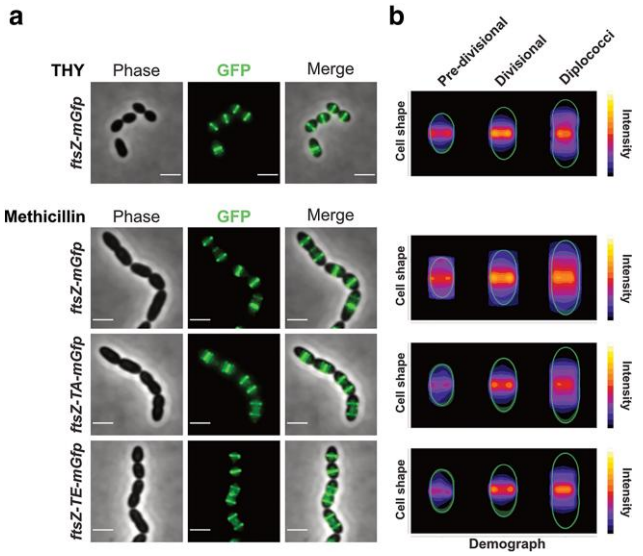

Figure 5 CTL phosphorylation does not affect FtsZ localization in the presence of methicillin. a) FtsZ-mGFP localization in WT and phosphomutant strains grown in the presence or absence of 50 ng mL^{-1} methicillin. The left panel displays representative phase-contrast microscopy images illustrating *ftsZ-mGfp*, *ftsZ-TA-mGfp*, and *ftsZ-TE-mGfp* cells. The middle panel presents GFP fluorescence images, and the right panel shows merged images of both phase-contrast and GFP images (scale bar, 1 μm). b) Cells are categorized into predivisional, divisional, and diplococci based on their cell length. The heat maps highlight FtsZ-mGFP localization patterns in WT and phosphomutant strains. Microscopy images and heat maps are derived from a single experiment that is consistent with observations from three independent experiments.

only ∼50% of cells exceeding the Q3 threshold, indicating substantial rescue of the division block (Fig. S5b). These results suggest that higher-order phosphomimetic combinations are required to overcome methicillin-induced inhibition of septation.

We then assessed whether the methicillin stress impacts the localization of FtsZ at the division septum. We first verified that the levels of the different FtsZ-mGFP fusions were similar in the presence of methicillin (Fig. S6a). As expected, *ftsZ-mGfp* and *ftsZ-TA-mGfp* cells exhibited cell elongation following methicillin treatment, identical to their native counterparts, whereas *ftsZ-TE-mGfp* cells demonstrated a partial alleviation of the block in cell division (Fig. S6b). Analysis of FtsZ localization showed that WT FtsZ-mGFP, FtsZ-TA-mGFP, and FtsZ-TE-mGFP remained localized at the division septum even in the presence of methicillin (Fig. 5a and b). To evaluate whether methicillin alters Z-ring condensation, we quantified Z-ring width by extracting fluorescence intensity profiles across the FtsZ-mGFP band and calculating the full width at half maximum (FWHM) for each cell. Methicillin-treated *ftsZ-TE-mGfp* cells exhibited slightly narrower Z-rings than WT or *ftsZ-TA-mGfp*, reflected by a modest left-shift in the Z-ring width distribution (Fig. S6c), consistent with the reduced cell area observed for the TE mutant. The data show that CTL phosphorylation partially rescues division and suggest that it finely modulates Z-ring condensation under conditions that inhibit PBP2x.

β-Lactam treatment triggers rapid phosphorylation of FtsZ

Since the phosphomimetic *ftsZ-TE* allele partially alleviated the methicillin-induced division block, we next examined whether β-lactam stress itself could trigger endogenous phosphorylation of FtsZ. Ampicillin, another β-lactam antibiotic, has previously been shown to increase the number of phosphorylation sites on FtsZ (32). We therefore first checked whether methicillin might similarly induce FtsZ phosphorylation. WT cells were exposed to either ampicillin or methicillin treatment, and the phosphoprotein patterns were analyzed by immunoblotting with phosphothreonine antibodies. Surprisingly, only marginal changes were detected upon methicillin treatment (Fig. S7a). In contrast, and consistent with earlier reports (32, 38), ampicillin

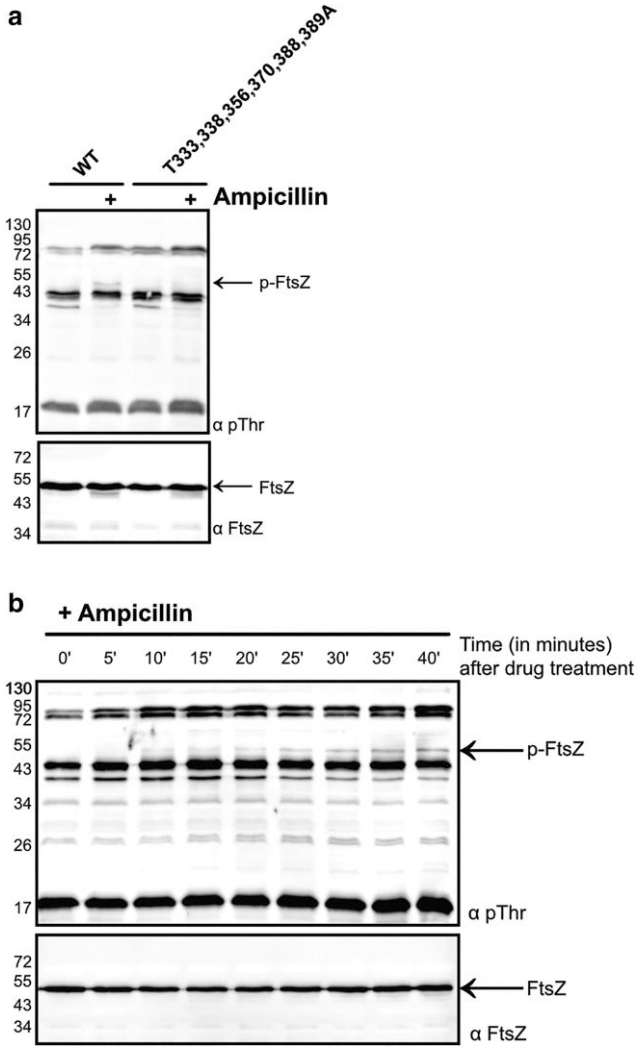

Figure 6 FtsZ phosphorylation dynamics during β-lactam antibiotic exposure. a) Western blot analysis of WT and the phosphoablative *ftsZ-TA* hexa mutant treated with ampicillin for 30 min. Untreated samples collected at the same stage served as controls. After incubation, cell-free extracts were prepared, and equal amounts of proteins were probed with anti–phosphothreonine (upper panel) and anti-FtsZ antibodies (lower panel), with FtsZ used as a loading control. b) Time-course analysis of FtsZ phosphorylation dynamics. Early-log WT cultures were treated with ampicillin, and cells were immediately harvested to obtain the 0-min time point. Samples were collected every 5 min up to 40 min, and cell-free extracts were probed with anti–phospho-threonine (upper panel) and anti-FtsZ antibodies (lower panel), with FtsZ serving as a loading control. In a and b, the ampicillin-induced phosphoprotein band is indicated with an arrow.

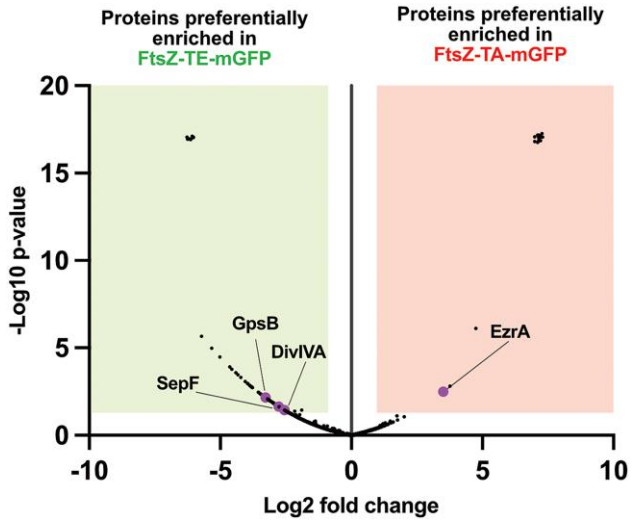

Figure 7 Proteomic analysis of FtsZ-TA-mGFP and FtsZ-TE-mGFP interaction partners. The volcano plot illustrates proteins that co-immunoprecipitated with either FtsZ-TA-mGFP or FtsZ-TE-mGFP, highlighting their preferential enrichment in each condition. Proteins enriched in the FtsZ-TA-mGFP pull-down are positioned on the right, while those enriched in the FtsZ-TE-mGFP pull-down are on the left. The data represent the average of three independent biological replicates. Proteins were deemed significantly enriched or depleted in the co-immunoprecipitated fractions if their fold change was >2 or <0.5, respectively, with a *P*-value of <0.05.

exposure resulted in the appearance of a distinct phosphoprotein band migrating at the expected molecular weight of FtsZ (Figs. 6a and S7a).

To determine whether this ampicillin-induced phosphorylation signal corresponded to FtsZ, we compared the phosphorylation patterns of WT cells and the *ftsZ-TA* mutant carrying the hexa threonine-to-alanine substitutions within the CTL (Fig. 6a). The distinct phosphoprotein band migrating at the FtsZ expected molecular weight was completely abolished in the *ftsZ-TA* mutant, identifying FtsZ as the phosphoprotein modified under ampicillin stress (Fig. 6A). Temporal analysis further revealed that FtsZ phosphorylation became detectable within 10 min of ampicillin exposure, reached approximately half-maximal intensity by 25 min, and continued to accumulate thereafter (Fig. 6b). Together, these results demonstrate that β-lactam treatment induces rapid phosphorylation of FtsZ in a manner that depends on the specific β-lactam used.

CTL phosphorylation alters FtsZ polymerization, treadmilling dynamics, and its interactome

To explore how the CTL phosphorylation affects cell division, we first investigated whether it may impact the FtsZ-related protein networks. Co-immunoprecipitation of FtsZ-TA-mGFP and FtsZ-TE-mGFP phosphomutants (Fig. S8), followed by MS, showed that the phosphoablative 6TA variant mainly associated with EzrA, while the phosphomimetic 6TE variant preferentially interacted with GpsB, SepF, and DivIVA (Fig. 7). These observations suggest that CTL phosphorylation state influences the FtsZ interaction profile.

Given prior studies that linked the CTL to lateral interactions established by FtsZ filaments (21), we also hypothesized that the negative charges introduced by phosphorylation might impact the FtsZ filament conformation. To investigate this, we first utilized the CIDER tool, developed to predict the behavior of intrinsically disordered peptides (55). Supporting our hypothesis, CIDER analysis predicted altered charge distribution and conformational states in the TE mutant relative to WT and TA variants (Fig. S9a–d). Consistent with the experimentally observed phosphorylation threshold needed for partial rescue from division arrest (Fig. S5a and b), CIDER analysis of single-to-hexa variants revealed predicted differences primarily for higher-order phosphomimetic substitutions (Fig. S11e and f). In

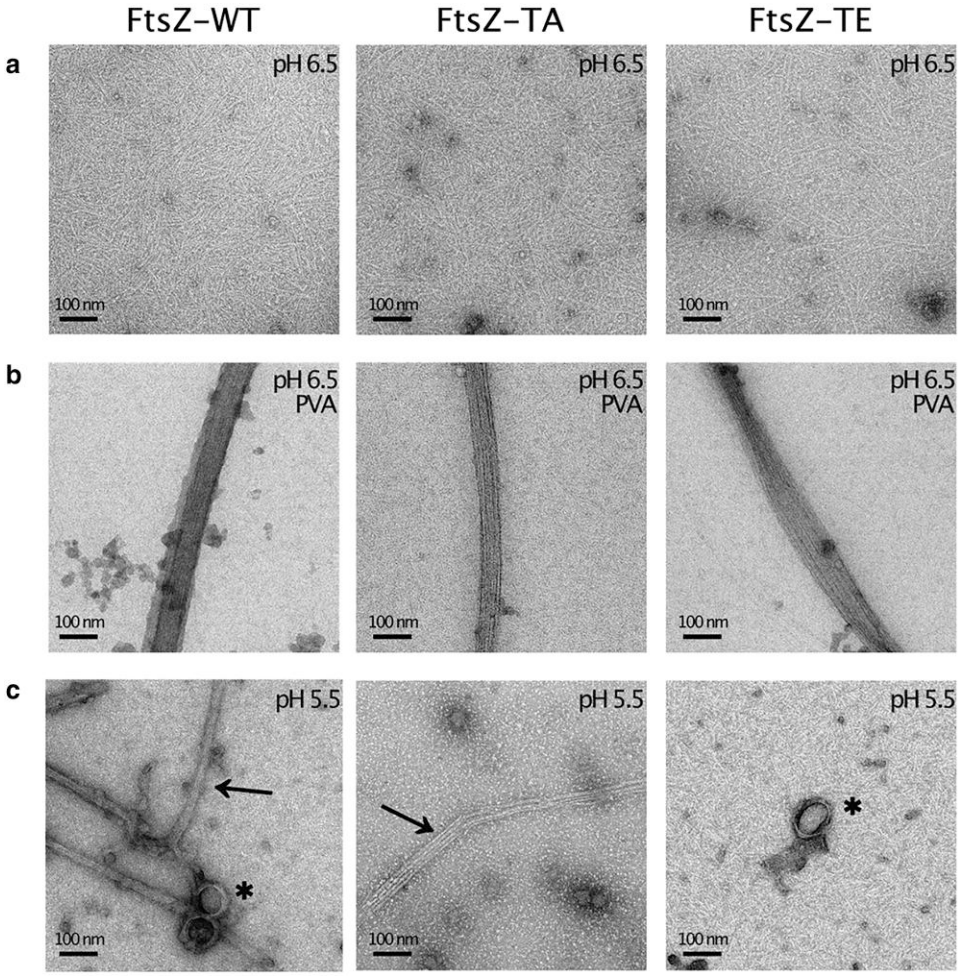

Figure 8 CTL phosphorylation modulates filament formation and bundling of FtsZ. Electron micrographs depicting the polymerization of WT and phosphomutant variants of FtsZ. Purified forms of WT and phosphomutant variants of FtsZ were polymerized at a concentration of 5 μM, either with or without a crowding agent (PVA). a) Transmission electron microscopy (TEM) images of the WT and phosphomutant variants were captured 15 min after adding GTP and subsequent staining with 1% uranyl acetate, highlighting the polymerization process at a pH of 6.5. b) TEM images illustrating polymerization at pH 6.5 in the presence of an 8% (wt/vol) PVA were similarly acquired 15 min after GTP addition and staining. c) TEM images displaying polymerization at a pH of 5.5 were also captured 15 min post-GTP addition, following staining with 1% uranyl acetate. For this experiment, a pH of 5.5 was achieved by introducing 0.125% (vol/vol) acetic acid, with no crowding agent included. Scale bars represent 100 nm. Arrow indicates long protofilaments. Asterisk represents curved bundles.

contrast, all phosphoablative variants exhibited similar behavior in the CIDER analysis (Figs. S10 and S11), and lower-order phosphomimetic mutants closely resembled their phosphoablative counterparts (Fig. S10 and S11a, d). To further investigate whether CTL phosphorylation affects the biophysical properties and dynamics of FtsZ, we performed polymerization and filament bundling assays using recombinant WT and phosphovariant forms of FtsZ (Figs. 8 and S12a). At pH 6.5, all FtsZ variants produced similar individual filaments or filament bundles, regardless of whether polyvinyl alcohol (PVA) was added (Figs. 8a, b and S13a, b). However, at pH 5.5, a condition that promotes bundling, interesting differences emerged (Figs. 8c and S13c). FtsZ-TA formed long, straight filament bundles with no additional filaments present in the background (Figs. 8c and S13c). In contrast, FtsZ-TE produced curved filaments alongside shorter, straight bundles in the background (Figs. 8c and S13c, d). WT FtsZ exhibited intermediate properties (Fig. 8c). Overall, these observations suggest that CTL phosphorylation modulates lateral FtsZ filament interactions and bundling under mild acidic conditions.

Since cell division involves FtsZ treadmilling, we next investigated whether the phosphorylation status of the CTL influences FtsZ movement in vivo. To achieve this, we performed total internal reflection fluorescence microscopy (TIRF) with FtsZ-mGFP and phospho-mutant variants and quantified treadmilling dynamics using kymograph analysis (Fig. 9a–c). Consistent with previous findings (28), WT FtsZ-mGFP treadmilled at 28.9 (±7.7) nm s^{-1}, while both TA and TE mutants exhibited significantly faster rates at 31.3 (±8.9) and 31.7 (±9.3) nm s^{-1}, respectively (Fig. 9d and e). Altogether, the phosphorylation status of the CTL influences filament interactions, FtsZ interactome and its treadmilling dynamics in living cells.

Discussion

Work in *E. coli*, *B. subtilis*, and *C. crescentus* has shown that the CTL modulates lateral interactions between FtsZ filaments, thereby regulating filament bundling and the formation of a dynamic Z-ring, which is essential for divisome assembly and

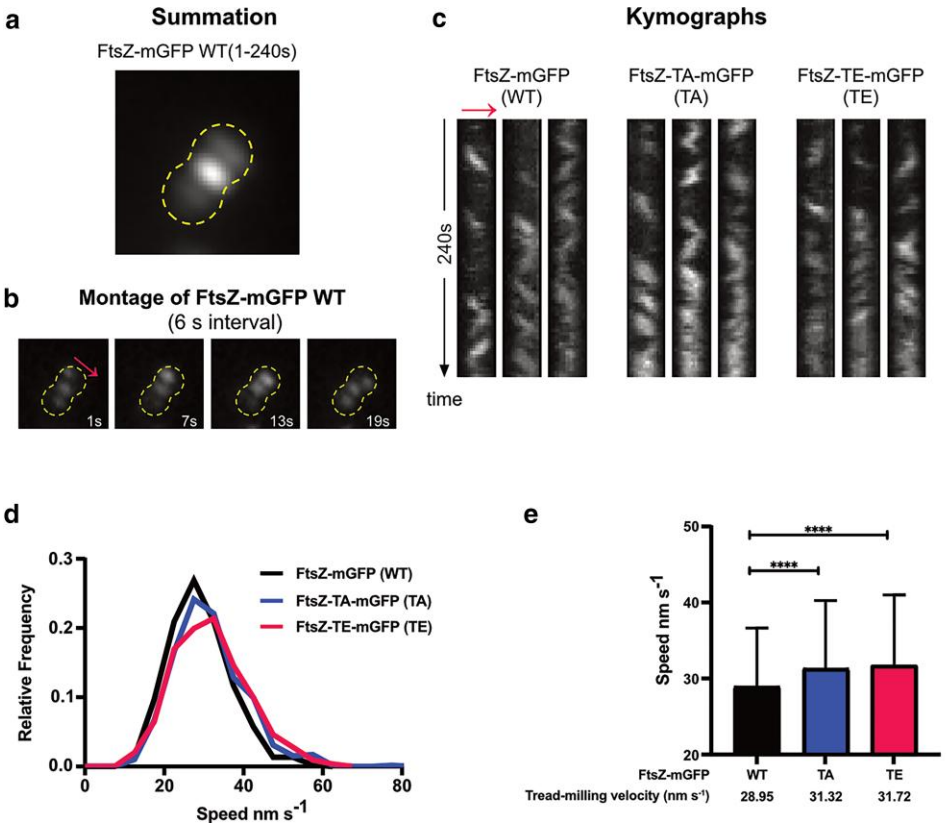

Figure 9 Phosphorylation alters FtsZ treadmilling. a) Summation of frames from 240-s TIRFM movies of *ftsZ-mGfp* (3-s intervals). The cell contour is indicated with yellow dotted lines. b) Montage of TIRFM images taken every 6 s, showing *ftsZ-mGfp* WT cells. The red arrow points to the trajectory used for the first kymograph analysis in (c) (moved slightly upward to help visualize FtsZ patches). c) Images of kymographs from 1 to 240 s, taken from *ftsZ-mGfp*, *ftsZ-TA-mGfp*, and *ftsZ-TE-mGfp* strains, with the red arrow indicating the trajectory shown in "b." d. Distribution of speeds of FtsZ-mGFP patches in WT, the phosphoablative mutant *ftsZ-TA*, and the phosphomimetic mutant *ftsZ-TE*. e) Average speed of FtsZ-mGFP patches in WT and phosphomutants. Results of the nonparametric Mann–Whitney test: ****$P < 0.0001$. The data presented corresponds to a representative experiment from three independent biological replicates, with a total of 1,610, 2,028, and 1,382 trajectories analyzed for the WT, *ftsZ-TA*, and *ftsZ-TE* mutants, respectively.

activity (13–15). Consistent with this, deletion of specific CTL regions in *S. pneumoniae* leads to a division block and subsequent cell elongation (Fig. 1). Despite its poor sequence conservation across species, the CTL thus likely functions as a conserved structural element mediating interactions required for divisome assembly and/or function.

Beyond confirming this structural role, our work examines how CTL phosphorylation influences FtsZ polymerization, dynamics, and cell morphogenesis. FtsZ phosphorylation has been documented in several bacterial species, typically on serine and threonine residues within flexible regions like the N-terminal loop and the CTL (30–36, 56–60). However, the regulatory roles of these phosphorylations remain unclear. In some organisms, phosphorylation within the GTP-binding core affects GTPase activity and, thereby, FtsZ polymerization, influencing cell growth and morphology as shown in *Deinococcus radiodurans* and *Mycobacterium* species (56, 57). Here, we identify six phosphorylated threonine residues in the *S. pneumoniae* FtsZ CTL, including four previously reported sites (T333, T338, T356, and T388) (31–33), and show that these posttranslational modifications affect FtsZ polymerization and filament bundling in vitro, as well as its interactome and treadmilling dynamics in vivo (Figs. 7–9). Our results indicate that the cumulative phosphorylation, rather than modification of any single threonine, is critical for modulating FtsZ function (Fig. S5). While the phosphoablative mutants fail to rescue division defects, higher-order phosphomimetic mutants achieve partial rescue, highlighting the importance of multiple sites acting in concert (Figs. 4 and S5b). Enhanced phosphorylation of several substrates (38), especially the FtsZ CTL (32), has been observed earlier when the pneumococcus was exposed to sublethal ampicillin concentrations, although the regulatory mechanism was not explored. Our results suggest that CTL phosphorylation influences cell shape (Fig. 2) and facilitates cell division under antibiotic stress (Fig. 4), thereby implicating it in an adaptive response. Whereas methicillin induced only marginal changes in FtsZ phosphorylation (Fig. S7a), ampicillin exposure produced distinct phosphoprotein bands (Fig. 6), including a discrete phosphospecies consistent with prior reports (38). This difference likely reflects methicillin's narrower inhibitory spectrum, which specifically targets PBP2x, compared with ampicillin's broader engagement of multiple PBPs and its ability to induce a stronger stress response. Ampicillin has also been shown to hyperactivate the Ser/Thr kinase StkP (32), potentially contributing to the robust phosphorylation observed, whereas whether methicillin similarly affects StkP remains unclear. Moreover, these findings imply that regardless of a β-lactam′s ability to promote FtsZ phosphorylation, modifying FtsZ biochemical properties, through phosphomimetic mutations, may alleviate the cell division block and associated cell elongation caused by any β-lactam. A possibility is that the CTL phosphorylation status

enhances the ability of the divisome to accomplish cell division upon impaired PG assembly. Further studies will be required to demonstrate this hypothesis.

The effects of CTL phosphorylation may arise from changes in filament flexibility and lateral interactions, which could alter contacts with Z-ring regulators, and thereby influence divisome assembly and activity. Supporting this, a recent work in *B. subtilis* has shown that phosphorylation in the FtsZ tail modulates tail–core interactions, thereby changing access to the polymerization interface and to division regulators (61). Lateral interactions among FtsZ filaments are essential for Z-ring assembly and dynamics, and CTL phosphorylation may modulate these interactions by reshaping FtsZ's associations with division partners. EzrA positively regulates Z-ring formation, while ZapA and ZapJ stabilize filaments; combined deletion of these proteins with EzrA leads to pronounced morphological defects (24). Supporting this mechanistic link, our interactome analysis shows that distinct CTL phosphorylation states shift FtsZ partner connectivity: the phosphoablative 6TA variant preferentially interacts with EzrA, whereas the phosphomimetic 6TE variant engages GpsB, SepF, and DivIVA (Fig. 7). These data suggest that CTL phosphorylation indirectly regulates filament organization and Z-ring assembly by modulating partner interactions, complementing the observed differences in filament bundling and treadmilling. Consistent with this idea, GpsB has recently been identified as an FtsZ-interacting protein in *S. pneumoniae*, where it serves as an accessory Z-ring anchor (62). In our study, this interaction is preferentially observed with the phosphomimetic 6TE variant, suggesting that CTL phosphorylation may bias FtsZ toward engagement with specific divisome partners. Single-molecule studies in *Bacillus* further support the importance of lateral interactions and Z-ring condensation for proper cell division (63), supporting the broader relevance of these interactions in bacterial cytokinesis. In *C. crescentus*, deleting the CTL disrupts lateral filament interactions and affects FtsA binding, which impairs PG synthesis and leads to cell lysis (64). In our study, the phosphomimetic *ftsZ-TE* mutant partially rescues exacerbated cell elongation caused by methicillin, which inhibits the essential septal PG synthase PBP2x in *S. pneumoniae* (Fig. 4) (27, 54, 65). These findings suggest that phosphorylation-dependent changes in FtsZ filament conformation may help *S. pneumoniae* balance cell elongation and division under adverse conditions, such as antibiotic exposure or nutrient deprivation (66, 67).

Such a mechanism may represent a broader adaptive strategy for antibiotic tolerance. In *E. coli*, the Ser/Thr kinase HipA phosphorylates glutamyl-tRNA-synthetase GltX, thereby inhibiting translation and promoting persistence (68). Similarly, in *S. aureus*, deletion of the Ser/Thr phosphatase Stp increases persistence by hyper-phosphorylating translational factors, such as EF-Tu (69). Although phosphorylation-mediated antibiotic tolerance remains unexplored in *S. pneumoniae*, phosphoproteomic analyses have shown increased phosphorylation of several division proteins, including MapZ, FtsZ, DivIVA, GpsB, MpgA, MacP, MurM, and the StkP kinase itself under ampicillin stress (32, 38). These observations support the idea that phosphorylation of cell division components, including FtsZ CTL, is part of a stress-adaptive program that may promote survival during antibiotic challenge.

Live-cell TIRF microscopy further supports this hypothesis by showing that CTL phosphorylation affects FtsZ treadmilling velocity (Fig. 9). Both FtsZ-TA and FtsZ-TE mutants exhibit faster treadmilling than the WT, indicating that precise phosphorylation levels are essential for optimal Z-ring dynamics. Although treadmilling organizes the spatial distribution of septal PG synthases, the rate of PG synthesis depends on synthase activity (28, 70). Notably, despite increased treadmilling in both mutants, only the phosphomimetic TE mutant confers protection to cells under antibiotic stress. This difference likely reflects additional contributions from filament polymerization and CTL-dependent interactions: TE forms shorter, more curved filaments with altered lateral associations and preferentially recruits divisome partners such as GpsB, DivIVA, and SepF, whereas TA filaments resemble WT and preferentially engage EzrA (Figs. 7–9). Together, these effects may enhance septal robustness, explaining why TE, but not TA, partially suppresses methicillin-induced elongation.

Our findings can be integrated into the "two-track" division model described in *E. coli*, in which inactive septal PG synthases are distributed around the division site by FtsZ treadmilling, before FtsN promotes their release from the Z-ring to initiate septal PG synthesis (71). In *S. pneumoniae*, this model is supported by the fact that the FtsZ treadmilling velocity does not correlate with the motion of FtsW/PBP2x complexes active in septal PG synthesis (28). In *S. pneumoniae*, it is plausible that FtsZ phosphorylation influences the recruitment of FtsW/PBP2x complexes or their release from the Z-ring, and thereby modulates active septal PG synthesis. The ability of FtsZ-TE to reduce cell elongation during methicillin treatment supports this model (Figs. 4 and S5), suggesting that enhanced phosphorylation of FtsZ may compensate for impaired septal PG synthesis.

An important unanswered question concerns the stoichiometry and dynamics of CTL phosphorylation. Our phosphomutants (FtsZ-TA and FtsZ-TE) represent extreme, nonphysiological states of FtsZ, whereas the native FtsZ is likely only partially and dynamically phosphorylated. Future studies should quantify the fraction of phosphorylated FtsZ protomers in filaments, determine whether phosphorylation occurs combinatorially across six phosphosites, and establish how these modifications fluctuate during the cell cycle. Regulation of FtsZ CTL phosphorylation by the StkP kinase and its cognate phosphatase PhpP may contribute to such dynamic control (37, 38).

In summary, our results highlight Ser/Thr phosphorylation as a crucial regulatory mechanism enabling bacteria to rapidly adapt to cell envelope stress. CTL phosphorylation of FtsZ occurs rapidly (Fig. 6), consistent with an early stress-response modification. Given the essential role of FtsZ in bacterial cell division and the conservation of CTL phosphorylation across species, this mechanism may represent a broadly conserved strategy to ensure division under challenging conditions. Further studies should investigate the additional roles of phosphorylation in regulating cell division and survival under various environmental stresses. Moreover, determining how these differential partner interactions contribute to the methicillin-rescue phenotype will be an important direction for future research.

Materials and methods

Strains and growth conditions

Streptococcus pneumoniae R800 and its derivatives (Table 1) were cultured in Todd–Hewitt yeast broth (THY; Difco) at 37 °C.

Recombinant proteins were produced using the *E. coli* strain AD494 (DE3) (Table 2), which was grown in Luria-Bertani (LB) broth. Growth was monitored by measuring optical density every 10 min using a JASCO V-630-BIO spectrophotometer at an OD_{600nm} for *E. coli* and an OD_{550nm} for *S. pneumoniae*, respectively. MICs were determined using broth microdilution.

Pneumococcal strain construction

Genomic modifications in *S. pneumoniae* were achieved through homologous recombination using a two-step procedure involving a bicistronic *kan-rpsL* gene cassette known as Janus (72), as previously described (42). The oligonucleotide primers used are described in Table 3. The native *ftsZ* gene or its *mGFP* fusions, along with associated mutations, were constructed at the endogenous chromosomal locus. This arrangement allowed for expression under the regulation of its own promoter, serving as the sole source of protein.

In the first step, the Janus cassette was inserted at the 3′ end of *ftsZ*, conferring kanamycin resistance and a dominant streptomycin sensitivity in the otherwise streptomycin-resistant R6 *rpsL1* strain (R800). In the subsequent step, polymerase chain reaction (PCR)-amplified DNA fragments containing the desired mutations or fusions, along with homologous upstream and downstream flanks, were transformed into the *ftsZ* Janus strain to create markerless mutants or fusions. Initially, the bacteria were cultured in THY at 37 °C until they reached early-log phase growth. The cells were then treated with 10 μM of synthetic competence-stimulating peptide to induce competence. After an incubation period of 10 min at 37 °C with the transformable DNA fragments, the temperature was lowered to 30 °C for 20 min. The transformants were then plated on THY agar, supplemented with 3% (v/v) defibrinated horse blood, and incubated for 120 min at 37 °C. Recombinant strains were selected by overlaying a 10-mL THY agar with the appropriate antibiotic (streptomycin) and incubating them overnight at 37 °C. The presence of the mutations was confirmed through locus PCR and sequencing.

Plasmid construction

DNA fragments were obtained through PCR using chromosomal DNA from the *S. pneumoniae* R800 strain WT or *S. pneumoniae* mutant strain harboring mutations in the CTL as a template. The oligonucleotide primers used for cloning are described in Table 3. To construct plasmids producing WT *ftsZ* and phospho-mutant *ftsZ-TA* and *ftsZ-TE*, the corresponding DNA fragments were cloned in the pT7-7 plasmid at *NdeI* and *HindIII* sites (73) without a histidine tag. The clones were verified through PCR and sequencing. All generated plasmids are listed in Table 4.

Protein purification

To purify FtsZ, the pT7-7 plasmids harboring WT and phospho-*ftsZ* mutants were transformed into *E. coli* AD494 competent cells selected on ampicillin-containing LB agar plates. A single colony was inoculated in 20 mL of LB medium supplemented with ampicillin and allowed to grow overnight. Overnight-grown culture was inoculated (1/100) into fresh 2 L LB broth, incubated at 37 °C, and grown until the OD_{600nm} reached 0.6. The culture was then induced with 1 mM IPTG (isopropyl-β-D-thiogalactoside) and allowed to grow for 2 h at 37 °C. The cells were harvested by centrifugation, and the pellets were resuspended in 5 mL buffer A (50 mM Tris-HCl, pH 8.0, 50 mM KCl, 1 mM ethylenediaminetetraacetic acid [EDTA], pH 8.0) containing 10 mg mL^{-1} lysozyme, 10 μg mL^{-1} DNase I, 100 μg mL^{-1} RNase A, and 1 μg mL^{-1} protease inhibitor cocktail (Roche). The cell suspension was incubated on ice for 30 min. After sonication and centrifugation, ammonium sulfate was added to the supernatant to a final concentration of 30%, and the mixture was stirred at 4 °C for 30 min. The mixture was then centrifuged at 25,000 × *g* for 30 min, and the pellets were retained and resuspended in 5 mL of buffer A. This was followed by dialysis against buffer A for 4 h at 4 °C. The supernatant was then applied to a HiTrap Q HP column (GE Healthcare). After extensive washing with five column volumes of buffer A, the protein was eluted with a 0–50% gradient of buffer B (buffer A + 1 M KCl). Peak fractions containing FtsZ were pooled and concentrated in Amicon filters (10 kDa cut-off). The concentrated lysate was injected into a GE-Hiload 16/600 Superdex 200 size-exclusion chromatography column. The FtsZ protein peaks were collected in buffer A and analyzed on sodium dodecyl sulfate–polyacrylamide gel electrophoresis (SDS–PAGE). Homogeneous fractions were collected and concentrated, as mentioned above. The final buffer consisted of 50 mM Tris-HCl (pH 8.0), 200 mM KCl, 1 mM EDTA, and 10% glycerol. Protein concentrations were determined using a Coomassie assay protein dosage reagent (Uptima), and proteins were then aliquoted and frozen at −80 °C.

Polymerization and bundling assays of FtsZ for negative-stain electron microscopy

Purified recombinant FtsZ samples (native form, TA, and TE variants) were diluted to 5 μM in 50 mM MES buffer at pH 6.5, containing 5 mM $MgCl_2$ and 50 mM KCl. In all samples, FtsZ polymerization was induced at room temperature by the addition of 5 mM GTP. FtsZ filament bundling was promoted by the presence of 8% (wt/vol) PVA or 0.125% (vol/vol) acetic acid, which decreased the pH of the reaction mix to 5.5. Samples were observed 15 min after the addition of GTP. For electron microscopy analysis, samples were absorbed on the clean side of a carbon film on mica, stained with 1% (wt/vol) uranyl acetate, and transferred to a 400-mesh copper grid. Images with underfocus values between 1.2 and 2.5 μm were captured on a Tecnai 12 FEI LaB6 electron microscope operating at an accelerating voltage of 120 kV. Image acquisition was performed with a nominal magnification of 23,000, using a CCD Gatan ORIUS SC1000 camera.

FtsZ immunoprecipitation and MS analysis

Culture of *S. pneumoniae* WT cells harboring *ftsZ-mGfp* was grown at 37 °C in THY until an absorbance of OD_{550} reached 0.3. Cell pellets were collected and incubated at 30 °C for 30 min in protoplast buffer A (0.1 M Tris-HCl, pH 7.5, 2 mM $MgCl_2$, 1 M sucrose, 10 μg mL^{-1} DNase I and 100 μg mL^{-1} RNase A). After centrifugation at 4 °C, the pellet was resuspended in hypotonic buffer B (0.1 M Tris-HCl, pH 7.5, 1 mM EDTA, 0.1%

Triton X-100, 10 µg mL^{-1} DNase I, and 100 µg mL^{-1} RNase A) and incubated for 15 min at room temperature before being harvested by centrifugation. Cell-free extracts were prepared by centrifugation for 30 min at 15,000 × *g* at 4 °C. The amount of protein was estimated using the Bradford method, and equal amounts were incubated with GFP-Trap_A beads (Chromtek) coupled with anti-GFP antibodies for 2 h at 4 °C. After extensive washing with buffer C (10 mM Tris-HCl, pH 7.5, 0.5 mM EDTA, 0.1% Triton X-100, and 150 mM NaCl), protein-bound beads were eluted with SDS–PAGE loading buffer at 95 °C for 10 min and analyzed by SDS–PAGE. Protease inhibitor (Roche) and phosphatase inhibitor (Sigma) cocktails were included at all steps. The FtsZ-mGFP bands from the WT cultures were excised from SDS–PAGE gels and analyzed by nano-LC-MS/MS. Detailed protocols for sample preparation, MS, and interactome experiments are provided in the Supplementary Material.

Immunoblot analysis

For immunoblot analysis, *S. pneumoniae* cells were resuspended in TE buffer (10 mM Tris-HCl, pH 8, and 1 mM EDTA) supplemented with a protease and phosphatase inhibitor cocktail (Sigma-Aldrich) and then lysed by sonication. Cell-free extracts (25 µg) were analyzed by SDS–PAGE and electrotransferred onto a polyvinylidene difluoride membrane. For FtsZ, immunodetection was performed using a specific rabbit polyclonal anti-ftsZ antibody at a dilution of 1:10,000 (74). GFP fusions were detected using rabbit anti-GFP antibodies at 1:10,000 (AMS Biotechnology). To detect endogenous phosphorylation patterns, rabbit polyclonal anti–phospho-threonine antibodies from Cell Signaling Technology were used at a 1:2,000 dilution. Five percent BSA was applied to block membranes before incubating them with anti–phospho-threonine antibodies. For loading controls, a rabbit anti-enolase polyclonal antibody at 1/500,000 was used (gift from C. Morlot's lab). A horseradish peroxidase-conjugated goat anti-rabbit polyclonal antibody (Bio-Rad) was used at a dilution of 1:5,000 to expose the immunoblots.

Peptidoglycan labeling with fluorescent D-amino acids

Newly synthesized PG was visualized under the microscope using fluorescently labeled D-amino acids (53). The BADA pulse labeling was carried out as previously described (44). Briefly, *S. pneumoniae* cells containing either the WT or phosphomutant variant FtsZ were grown exponentially in the THY until the absorbance at OD_{550nm} reached 0.1. One milliliter of cell culture was incubated for 5 min at 37 °C in the presence of 500 µM BADA (4,4-Difluoro-5,7-Dimethyl-4-Bora-3a,4a-Diaza-s-Indacene-3-PropionicAcid-3-amino-D-alanine). The cells were washed three times with 1 mL of PBS (pH 7.4), resuspended in 0.1 mL of PBS, and then observed under the microscope.

Microscopy techniques and image analysis

Cells were grown in THY at 37 °C to exponential growth (OD_{550} = 0.1). Then, cells were diluted to an initial OD_{550} = 0.02 in fresh THY in absence or presence of 50 ng mL^{-1} methicillin and grown until OD_{550} = 0.10–0.15 (∼120 min), at which point they were harvested for imaging. Glass slides with an agarose pad were spotted with 1.0 µL of the cell suspension. Slides were visualized with a Nikon TiE microscope fitted with an Orca-CMOS Flash4 V2 camera with a 100 × 1.45 objective. Images were collected using NIS-Elements (Nikon). Images were analyzed using Fiji (ImageJ; http://rsb.info.nih.gov/ij/) with the MicrobeJ plugin (75). Individual cells were automatically segmented from phase-contrast images, using the MicrobeJ cell detection module based on intensity thresholding and subpixel contour detection. A minimal cell-width cut-off was defined to preferentially segment single cells and minimize the inclusion of cell chains. Segmented objects were further filtered using morphology-based criteria (e.g. area and solidity) to exclude debris and improperly segmented cells. A medial axis was extracted for each retained cell to enable subcellular localization and quantitative analysis. FtsZ-mGFP localization or PG labeling was detected using the feature/patch detection option in MicrobeJ. This approach combines spatial 2D filtering (using a Median Filter) with a 2D local maxima algorithm to identify individual fluorescent maxima within each detected cell. Detected maxima were then fitted to a single peak or a multipeak 2D Gaussian models to determine their amplitude, FWHM, and subpixel coordinates. Maxima were finally filtered based on fit quality and amplitude, and their subcellular localizations were automatically computed for each associated particle.

For total TIRF microscopy

Cultures of *S. pneumoniae* cells harboring *ftsZ-mGfp* WT or *ftsZ-TA/TE-mGfp* variants were grown at 37 °C to an OD_{550} of 0.15 in C + Y medium. These precultures were inoculated again (1/15) in C + Y medium and incubated at 37 °C to an optical density at 550 nm (OD_{550}) of 0.15. Before imaging, 0.8 µL of this suspension was immobilized on a 1.2% C + Y agarose-coated microscope slide with a cover glass (# 1.5). All TIRF time-lapses were acquired at 37 °C on an automated Zeiss Elyra PS1 microscope with a climate control chamber equipped with a 100×/1.46 NA Apochromat oil immersion objective. Laser excitation at 488 nm was set at 10% of the maximum excitation power, with an exposure time of 100 ms. Images were collected using an electron-multiplying charge-coupled device (emCCD) camera (Andor iXon) with electron-multiplying gains (300×) and a 2.5× magnification lens. Acquisition was controlled by the Zen Software (Zeiss) software package. Velocity measurements of dynamic proteins were performed, as previously described (76). All statistical analyses were performed with Prism 10 (GraphPad Software, LLC). Pairwise comparison between two conditions was realized with a nonparametric Mann–Whitney test, *P* values are displayed as follows: ****$P < 0.0001$; ***$P < 0.001$; **$P < 0.01$; *$P < 0.05$; ns, $P > 0.05$.

Acknowledgments

The authors acknowledge the contribution of the Protein Science Facility of the "Structure Féderative de Recherche" Biosciences Gerland-Lyon-Sud (UAR344/US8), especially Adeline Page and Frédéric Delolme, for the MS analyses. They gratefully

acknowledge support from the CNRS/IN2P3 Computing Center (Lyon, France) for providing computing and data-processing resources needed for this work. They also thank the Proteomics Core Facility, Sahlgrenska Academy, University of Gothenburg, Gothenburg, Sweden, for help with the LC-MS/MS analysis. They want to thank Adrien Ducret and Veruca Ulm for expert assistance with MicrobeJ and stimulating discussions, respectively.

Supplementary material

Supplementary material is available at *PNAS Nexus* online.

Competing interests

The authors declare no competing interests.

Funding

This project was supported by grants from the Agence Nationale de la Recherche (contracts ANR-18-CE11-0017-02 and ANR-24-CE11-4058-02 to C.G. and ANR-23-CE11-0029 to C.M.), the Fondation pour la Recherche Médicale (FRM EQU202103012753) to C.G., and the Novo Nordisk Foundation (NNF20CC0035580) and Vetenskapsrådet (2020-03176) to I.M. It was also supported by grants from the Centre National de la Recherche Scientifique, Université Claude Bernard Lyon 1, and the Bettencourt Schueller Foundation to C.G. IBS acknowledges integration into the Interdisciplinary Research Institute of Grenoble (IRIG, CEA). This work used the platforms of the Grenoble Instruct-ERIC center (ISBG; UMS 3518 CNRS-CEA-UGA-EMBL) within the Grenoble Partnership for Structural Biology (PSB), supported by FRISBI (ANR-10-INBS-05-02) and the LabEx GRAL (ANR-10-LABX-49-01), financed within the Université Grenoble Alpes graduate school (Ecoles Universitaires de Recherche) CBH-EUR-GS (ANR-17-EURE-0003). The IBS/ISBG electron microscope facility is supported by the Auvergne-Rhône-Alpes Region, the Fondation pour la Recherche Médicale (FRM), the European Regional Development Funds, and the Infrastructures en Biologie Santé et Agronomie (IBiSA).

Author contributions

Sathya Narayanan Nagarajan (Conceptualization, Data curation, Formal analysis, Investigation, Writing—original draft, Writing—review & editing), Sylvie Manuse (Formal analysis, Investigation, Methodology, Writing—review & editing), Dimitri Juillot (Conceptualization, Formal analysis, Investigation, Writing—review & editing), Léo Claude (Formal analysis, Methodology), Vaishnavi Ravikumar (Formal analysis, Investigation, Writing—review & editing), Emmanuelle Neumann (Formal analysis, Investigation, Writing—review & editing), Jean-Pierre Lavergne (Formal analysis, Investigation, Writing—review & editing), Mirita Franz-Wachtel (Formal analysis, Investigation, Writing—review & editing), Boris Macek (Formal analysis, Supervision, Writing—review & editing), Ivan Mijakovic (Formal analysis, Funding acquisition, Supervision, Writing—review & editing), Cecile Morlot (Formal analysis, Funding acquisition, Investigation, Writing—review & editing), Rut Carballido-Lopez (Formal analysis, Supervision, Writing—review & editing), and Christophe Grangeasse (Conceptualization, Formal analysis, Funding acquisition, Project administration, Supervision, Validation, Writing—original draft, Writing—review & editing)

Data availability

The MS phosphoproteomics data have been deposited to the ProteomeXchange Consortium via the PRIDE (77) partner repository with the dataset identifier PXD052685 and represent a subset of the recently published dataset (78, 79). The MS proteomics data have been deposited to the Center for Computational Mass Spectrometry repository (University of California, San Diego) via the MassIVE tool with the dataset identifier MassIVE MSV000100256.

References

1. Bi EF, Lutkenhaus J. 1991. Ftsz ring structure associated with division in *Escherichia coli*. *Nature*. 354:161–164.
2. Margolin W. 2005. FtsZ and the division of prokaryotic cells and organelles. *Nat Rev Mol Cell Biol*. 6:862–871.
3. RayChaudhuri D, Park JT. 1992. *Escherichia coli* cell-division gene ftsZ encodes a novel GTP-binding protein. *Nature*. 359:251–254.
4. Bramhill D, Thompson CM. 1994. GTP-dependent polymerization of *Escherichia coli* FtsZ protein to form tubules. *Proc Natl Acad Sci U S A*. 91:5813–5817.
5. Szwedziak P, Wang Q, Bharat TAM, Tsim M, Löwe J. 2014. Architecture of the ring formed by the tubulin homologue FtsZ in bacterial cell division. *Elife*. 3:e04601.
6. Yang X, *et al.* 2017. GTPase activity–coupled treadmilling of the bacterial tubulin FtsZ organizes septal cell wall synthesis. *Science*. 355:744–747.
7. Bisson-Filho AW, *et al.* 2017. Treadmilling by FtsZ filaments drives peptidoglycan synthesis and bacterial cell division. *Science*. 355:739–743.
8. Jacq M, *et al.* 2015. Remodeling of the Z-ring nanostructure during the Streptococcus pneumoniae cell cycle revealed by photoactivated localization microscopy. *mBio*. 6: e01108-15.
9. Erickson HP, Anderson DE, Osawa M. 2010. Ftsz in bacterial cytokinesis: cytoskeleton and force generator all in one. *Microbiol Mol Biol Rev*. 74:504–528.
10. Massidda O, Nováková L, Vollmer W. 2013. From models to pathogens: how much have we learned about *Streptococcus pneumoniae* cell division? *Environ Microbiol*. 15:3133–3157.
11. Vaughan S, Wickstead B, Gull K, Addinall SG. 2004. Molecular evolution of FtsZ protein sequences encoded within the genomes of archaea, bacteria, and eukaryota. *J Mol Evol*. 58: 19–29.
12. Lara B, *et al.* 2005. Cell division in cocci: localization and properties of the *Streptococcus pneumoniae* FtsA protein. *Mol Microbiol*. 55:699–711.

13. Buske PJ, Levin PA. 2013. A flexible C-terminal linker is required for proper FtsZ assembly in vitro and cytokinetic ring formation in vivo. *Mol Microbiol*. 89:249–263.
14. Gardner KAJA, Moore DA, Erickson HP. 2013. The C-terminal linker of *Escherichia coli* FtsZ functions as an intrinsically disordered peptide. *Mol Microbiol*. 89:264–275.
15. Sundararajan K, *et al.* 2015. The bacterial tubulin FtsZ requires its intrinsically disordered linker to direct robust cell wall construction. *Nat Commun*. 6:7281.
16. Buske PJ, Mittal A, Pappu RV, Levin PA. 2015. An intrinsically disordered linker plays a critical role in bacterial cell division. *Semin Cell Dev Biol*. 37:3–10.
17. Babu MM. 2016. The contribution of intrinsically disordered regions to protein function, cellular complexity, and human disease. *Biochem Soc Trans*. 44:1185–1200.
18. Popp D, Iwasa M, Narita A, Erickson HP, Maéda Y. 2009. Ftsz condensates: an in vitro electron microscopy study. *Biopolymers*. 91:340–350.
19. Alberti S, Gladfelter A, Mittag T. 2019. Considerations and challenges in studying liquid-liquid phase separation and biomolecular condensates. *Cell*. 176:419–434.
20. Shinn MK, *et al.* 2022. Connecting sequence features within the disordered C-terminal linker of *Bacillus subtilis* FtsZ to functions and bacterial cell division. *Proc Natl Acad Sci U S A*. 119:e2211178119.
21. Sundararajan K, Goley ED. 2017. The intrinsically disordered C-terminal linker of FtsZ regulates protofilament dynamics and superstructure in vitro. *J Biol Chem*. 292:20509–20527.
22. Huecas S, *et al.* 2017. Self-organization of FtsZ polymers in solution reveals spacer role of the disordered C-terminal tail. *Biophys J*. 113:1831–1844.
23. Pinho MG, Kjos M, Veening J-W. 2013. How to get (a)round: mechanisms controlling growth and division of coccoid bacteria. *Nat Rev Microbiol*. 11:601–614.
24. Perez AJ, *et al.* 2021. FtsZ-ring regulation and cell division are mediated by essential EzrA and accessory proteins ZapA and ZapJ in *Streptococcus pneumoniae*. *Front Microbiol*. 12: 780864.
25. Fleurie A, *et al.* 2014. Interplay of the serine/threonine-kinase StkP and the paralogs DivIVA and GpsB in pneumococcal cell elongation and division. *PLoS Genet*. 10:e1004275.
26. Trouve J, *et al.* 2021. Nanoscale dynamics of peptidoglycan assembly during the cell cycle of *Streptococcus pneumoniae*. *Curr Biol*. 31:2844–2856.e6.
27. Land AD, *et al.* 2013. Requirement of essential Pbp2x and GpsB for septal ring closure in *Streptococcus pneumoniae* D39. *Mol Microbiol*. 90:939–955.
28. Perez AJ, *et al.* 2019. Movement dynamics of divisome proteins and PBP2x: FtsW in cells of *Streptococcus pneumoniae*. *Proc Natl Acad Sci U S A*. 116:3211–3220.
29. Barrows JM, Goley ED. 2021. Ftsz dynamics in bacterial division: what, how, and why? *Curr Opin Cell Biol*. 68:163–172.
30. Giefing C, Jelencsics KE, Gelbmann D, Senn BM, Nagy E. 2010. The pneumococcal eukaryotic-type serine/threonine protein kinase StkP co-localizes with the cell division apparatus and interacts with FtsZ in vitro. *Microbiology*. 156:1697–1707.
31. Hirschfeld C, *et al.* 2019. Proteomic investigation uncovers potential targets and target sites of pneumococcal serine-threonine kinase StkP and phosphatase PhpP. *Front Microbiol*. 10:3101.
32. Ulrych A, *et al.* 2021. Cell wall stress stimulates the activity of the protein kinase StkP of *Streptococcus pneumoniae*, leading to multiple phosphorylation. *J Mol Biol*. 433:167319.
33. Lavergne J-P, Page A, Polard P, Campo N, Grangeasse C. 2025. Quantitative phosphoproteomic reveals that the induction of competence modulates protein phosphorylation in *Streptococcus pneumonaie*. *J Proteomics*. 315:105399.
34. Prisic S, *et al.* 2010. Extensive phosphorylation with overlapping specificity by *Mycobacterium tuberculosis* serine/threonine protein kinases. *Proc Natl Acad Sci U S A*. 107:7521–7526.
35. Ravikumar V, *et al.* 2014. Quantitative phosphoproteome analysis of *Bacillus subtilis* reveals novel substrates of the kinase PrkC and phosphatase PrpC. *Mol Cell Proteomics*. 13: 1965–1978.
36. Rioseras B, *et al.* 2018. Quantitative proteome and phosphoproteome analyses of *Streptomyces coelicolor* reveal proteins and phosphoproteins modulating differentiation and secondary metabolism. *Mol Cell Proteomics*. 17:1591–1611.
37. Nováková L, *et al.* 2005. Characterization of a eukaryotic type serine/threonine protein kinase and protein phosphatase of *Streptococcus pneumoniae* and identification of kinase substrates. *FEBS J*. 272:1243–1254.
38. Beilharz K, *et al.* 2012. Control of cell division in Streptococcus pneumoniae by the conserved Ser/Thr protein kinase StkP. *Proc Natl Acad Sci U S A*. 109:E905–E913.
39. Zucchini L, *et al.* 2018. PASTA repeats of the protein kinase StkP interconnect cell constriction and separation of *Streptococcus pneumoniae*. *Nat Microbiol*. 3:197–209.
40. Manuse S, Fleurie A, Zucchini L, Lesterlin C, Grangeasse C. 2016. Role of eukaryotic-like serine/threonine kinases in bacterial cell division and morphogenesis. *FEMS Microbiol Rev*. 40:41–56.
41. Nagarajan SN, Lenoir C, Grangeasse C. 2022. Recent advances in bacterial signaling by serine/threonine protein kinases. *Trends Microbiol*. 30:553–566.
42. Fleurie A, *et al.* 2012. Mutational dissection of the S/T-kinase StkP reveals crucial roles in cell division of *Streptococcus pneumoniae*: role of StkP in *Streptococcus pneumoniae*. *Mol Microbiol*. 83:746–758.
43. Fenton AK, *et al.* 2018. Phosphorylation-dependent activation of the cell wall synthase PBP2a in *Streptococcus pneumoniae* by MacP. *Proc Natl Acad Sci U S A*. 115:2812–2817.
44. Fleurie A, *et al.* 2014. Mapz marks the division sites and positions FtsZ rings in *Streptococcus pneumoniae*. *Nature*. 516: 259–262.
45. Holečková N, *et al.* 2014. Locz is a new cell division protein involved in proper septum placement in *Streptococcus pneumoniae*. *mBio*. 6:e01700–e01714.
46. Ulrych A, *et al.* 2016. Characterization of pneumococcal Ser/Thr protein phosphatase phpP mutant and identification of a novel PhpP substrate, putative RNA binding protein Jag. *BMC Microbiol*. 16:247.
47. Zheng JJ, Perez AJ, Tsui H-CT, Massidda O, Winkler ME. 2017. Absence of the KhpA and KhpB (JAG/EloR) RNA-binding proteins suppresses the requirement for PBP2b by overproduction of FtsA in *Streptococcus pneumoniae* D39. *Mol Microbiol*. 106:793–814.
48. Stamsås GA, *et al.* 2017. Identification of EloR (Spr1851) as a regulator of cell elongation in *Streptococcus pneumoniae*. *Mol Microbiol*. 105:954–967.

49. Demuysere M, Ducret A, Grangeasse C. 2024. Molecular dissection of the chromosome partitioning protein RocS and regulation by phosphorylation. *J Bacteriol*. 206:e00291-24.
50. Das RK, Huang Y, Phillips AH, Kriwacki RW, Pappu RV. 2016. Cryptic sequence features within the disordered protein p27Kip1 regulate cell cycle signaling. *Proc Natl Acad Sci U S A*. 113:5616–5621.
51. Lin Y, Currie SL, Rosen MK. 2017. Intrinsically disordered sequences enable modulation of protein phase separation through distributed tyrosine motifs. *J Biol Chem*. 292: 19110–19120.
52. Kuru E, Tekkam S, Hall E, Brun YV, Van Nieuwenhze MS. 2015. Synthesis of fluorescent D-amino acids and their use for probing peptidoglycan synthesis and bacterial growth in situ. *Nat Protoc*. 10:33–52.
53. Kuru E, *et al.* 2019. Mechanisms of incorporation for D-amino acid probes that target peptidoglycan biosynthesis. *ACS Chem Biol*. 14:2745–2756.
54. Kocaoglu O, Tsui H-CT, Winkler ME, Carlson EE. 2015. Profiling of β-lactam selectivity for penicillin-binding proteins in *Streptococcus pneumoniae* D39. *Antimicrob Agents Chemother*. 59:3548–3555.
55. Holehouse AS, Das RK, Ahad JN, Richardson MOG, Pappu RV. 2017. CIDER: resources to analyze sequence-ensemble relationships of intrinsically disordered proteins. *Biophys J*. 112:16–21.
56. Maurya GK, *et al.* 2018. Phosphorylation of FtsZ and FtsA by a DNA damage-responsive Ser/Thr protein kinase affects their functional interactions in *Deinococcus radiodurans*. *mSphere*. 3:e00325-18.
57. Thakur M, Chakraborti PK. 2006. GTPase activity of mycobacterial FtsZ is impaired due to its transphosphorylation by the eukaryotic-type Ser/Thr kinase, PknA. *J Biol Chem*. 281: 40107–40113.
58. Hardt P, *et al.* 2017. The cell wall precursor lipid II acts as a molecular signal for the Ser/Thr kinase PknB of *Staphylococcus aureus*. *Int J Med Microbiol*. 307:1–10.
59. Schultz C, *et al.* 2009. Genetic and biochemical analysis of the serine/threonine protein kinases PknA, PknB, PknG and PknL of *Corynebacterium glutamicum*: evidence for non-essentiality and for phosphorylation of OdhI and FtsZ by multiple kinases. *Mol Microbiol*. 74:724–741.
60. Manteca A, Ye J, Sánchez J, Jensen ON. 2011. Phosphoproteome analysis of *Streptomyces* development reveals extensive protein phosphorylation accompanying bacterial differentiation. *J Proteome Res*. 10:5481–5492.
61. Mallard WJ, Pham VV. 2025. Ftsz phosphorylation modulates tail-core binding to tune cell division in *Bacillus subtilis*. *PLoS One*. 20:e0337820.
62. Bhattacharya D, King A, McKnight L, Horigian P, Eswara PJ. 2025. Gpsb interacts with FtsZ in multiple species and may serve as an accessory Z-ring anchor. *Mol Biol Cell*. 36:ar10.
63. Squyres GR, *et al.* 2021. Single-molecule imaging reveals that Z-ring condensation is essential for cell division in *Bacillus subtilis*. *Nat Microbiol*. 6:553–562.
64. Barrows JM, Sundararajan K, Bhargava A, Goley ED. 2020. Ftsa regulates Z-ring morphology and cell wall metabolism in an FtsZ C-terminal linker-dependent manner in *Caulobacter crescentus*. *J Bacteriol*. 202:e00693-19.
65. Berg KH, Stamsås GA, Straume D, Håvarstein LS. 2013. Effects of low PBP2b levels on cell morphology and peptidoglycan composition in *Streptococcus pneumoniae* R6. *J Bacteriol*. 195:4342–4354.
66. Sperber AM, Herman JK. 2017. Metabolism shapes the cell. *J Bacteriol*. 199:e00039-17.
67. Yao Z, Davis RM, Kishony R, Kahne D, Ruiz N. 2012. Regulation of cell size in response to nutrient availability by fatty acid biosynthesis in *Escherichia coli*. *Proc Natl Acad Sci U S A*. 109:E2561–E2568.
68. Kaspy I, *et al.* 2013. HipA-mediated antibiotic persistence via phosphorylation of the glutamyl-tRNA-synthetase. *Nat Commun*. 4:3001.
69. Huemer M, *et al.* 2023. Serine-threonine phosphoregulation by PknB and Stp contributes to quiescence and antibiotic tolerance in *Staphylococcus aureus*. *Sci Signal*. 16:eabj8194.
70. Hu L, *et al.* 2025. FtsZ-mediated spatial–temporal control over septal cell wall synthesis. *Proc Natl Acad Sci U S A*. 122:e2426431122.
71. Yang X, *et al.* 2021. A two-track model for the spatiotemporal coordination of bacterial septal cell wall synthesis revealed by single-molecule imaging of FtsW. *Nat Microbiol*. 6:584–593.
72. Sung CK, Li H, Claverys JP, Morrison DA. 2001. An rpsL Cassette, Janus, for gene replacement through negative selection in *Streptococcus pneumoniae*. *Appl Environ Microbiol*. 67:5190–5196.
73. Cortay JC, *et al.* 1994. In vitro asymmetric binding of the pleiotropic regulatory protein, FruR, to the ace operator controlling glyoxylate shunt enzyme synthesis. *J Biol Chem*. 269: 14885–14891.
74. Morlot C, Zapun A, Dideberg O, Vernet T. 2003. Growth and division of *Streptococcus pneumoniae*: localization of the high molecular weight penicillin-binding proteins during the cell cycle. *Mol Microbiol*. 50:845–855.
75. Ducret A, Quardokus EM, Brun YV. 2016. Microbej, a tool for high throughput bacterial cell detection and quantitative analysis. *Nat Microbiol*. 1:16077.
76. Juillot D, *et al.* 2025. Transient inhibition of cell division in competent pneumococcal cells results from deceleration of the septal peptidoglycan complex. *Nat Commun*. 16:5666. https://doi.org/10.1038/s41467-025-60600-z.
77. Deutsch EW, *et al.* 2023. The ProteomeXchange consortium at 10 years: 2023 update. *Nucleic Acids Res*. 51:D1539–D1548.
78. Hamidi M, *et al.* 2025. The juxtamembrane domain of StkP is phosphorylated and influences cell division in *Streptococcus pneumoniae*. *mBio*. 16:e03799-24. https://doi.org/10.1128/mbio.03799-24
79. Hamidi M. (2025) Etude des mécanismes d'activation de la sérine/thréonine-kinase StkP et régulation de la division cellulaire chez la bactérie Streptococcus pneumoniae. Biologie Moléculaire. Université Claude Bernard—Lyon I, 2025. Français. NNT: 2025LYO10122. tel-05299499.